

Frequency-wavenumber migration for orthogonal plane wave imaging using row-column-addressed arrays

Jia Liu(刘佳), Chen Jiang(江晨), Chengcheng Liu(刘成成), Kailiang Xu(许凯亮), Dean Ta(他得安)
Citation: Chin. Phys. B. 35, 094302 (2026). DOI: 10.1088/1674-1056/ae1e67 | CSTR: 32038.14.CPB.ae1e67
http://cpb.iphy.ac.cn; http://iopscience.iop.org/cpb

What follows is a list of articles you may be interested in

Three-dimensional frequency-wavenumber method for efficient and high-quality volumetric ultrasound imaging

Huchang Guan(关虎昌), Chen Jiang(江晨), Kailiang Xu(许凯亮), Dean Ta(他得安)
Chin. Phys. B. 35, 074301 (2026). DOI: 10.1088/1674-1056/ae42b9 | CSTR: 32038.14.CPB.ae42b9

Comparing distinct dissociation pathways of Unexpected text node: '<' under laser and electron impact

Xiangjie Chen(陈祥杰), Jianting Lei(雷建廷), Chenyu Tao(陶琛玉), Shuncheng Yan(闫顺成), Yongzhe Ma(马永哲), Fenghao Sun(孙烽豪), Qingcao Liu(刘情操), Shaofeng Zhang(张少锋)
Chin. Phys. B. 35, 043202 (2026). DOI: 10.1088/1674-1056/ae311d | CSTR: 32038.14.CPB.ae311d

A WKB method based on parabolic cylinder function for very-low-frequency sound propagation in deep ocean

Jian-Kang Zhan(詹建康), Sheng-Chun Piao(朴胜春), Li-Jia Gong(龚李佳), Yang Dong(董阳), Yong-Chao Guo(郭永超), Guang-Xue Zheng(郑广学)
Chin. Phys. B. 34, 034301 (2025). DOI: 10.1088/1674-1056/ada886 | CSTR: 32038.14.CPB.ada886

Discrete multi-step phase hologram for high frequency acoustic modulation

Meng-Qing Zhou(周梦晴), Zhao-Xi Li(李照希), Yi Li(李怡), Ye-Cheng Wang(王业成), Juan Zhang(张娟), Dong-Dong Chen(谌东东), Yi Quan(全熠), Yin-Tang Yang(杨银堂), Chun-Long Fei(费春龙)
Chin. Phys. B. 33, 014303 (2024). DOI: 10.1088/1674-1056/acf44c

Simulation research on effect of magnetic nanoparticles on physical process of magneto-acoustic tomography with magnetic induction

Xiao-Heng Yan(闫孝姮), Ying Zhang(张莹), Guo-Qiang Liu(刘国强)
Chin. Phys. B. 27, 104302 (2018). DOI: 10.1088/1674-1056/27/10/104302

Frequency–wavenumber migration for orthogonal plane wave imaging using row–column-addressed arrays

Jia Liu(刘佳)[1,2,†], Chen Jiang(江晨)[1,†,‡], Chengcheng Liu(刘成成)[2], Kailiang Xu(许凯亮)[3,§], and Dean Ta(他得安)[1,2,3]

[1] *Yiwu Research Institute of Fudan University, Yiwu* 322000, *China*
[2] *School of Information Science and Technology, Fudan University, Shanghai* 200438, *China*
[3] *State Key Laboratory of Integrated Chips and Systems, Fudan University, Shanghai* 201203, *China*

(Received 7 August 2025; revised manuscript received 15 October 2025; accepted manuscript online 12 November 2025)

Row–column-addressed (RCA) arrays, composed of two orthogonal linear arrays with elongated elements, enable three-dimensional (3D) imaging with a larger aperture and fewer channels than conventional matrix arrays. Orthogonal plane-wave (OPW) coherent compounding is a specialized insonation mode for RCA arrays, characterized by the emission of orthogonally tilted plane waves and the coherent compounding of echo data to generate 3D images. Nevertheless, 3D beamforming is computationally expensive when using the conventional delay-and-sum algorithm. Frequency–wavenumber (F-K) beamformers are highly efficient beamforming solutions and have been widely investigated for two-dimensional (2D) imaging using linear arrays and for 3D imaging with matrix arrays. In contrast, the F-K beamformer for RCA-based OPW imaging remains to be further developed. In this work, an F-K domain beamforming strategy (OPW f-k) is proposed for efficient volumetric image reconstruction in RCA-based OPW imaging. The proposed method achieves a computational complexity of $O(PMH^2\log_2(MH))$ compared to $O(PNMH^2)$ required by the conventional delay-and-sum algorithm, resulting in an 11-fold processing time reduction on a CPU-based MATLAB platform. Besides, simulation and phantom experimental results indicate that OPW f-k can improve imaging quality, with quantitative evaluations demonstrating enhanced spatial resolution (2.19% reduction in full width at half maximum), contrast ratio (12.96% increase), and contrast-to-noise ratio (17.84% increase) compared to OPW DAS. In vivo carotid artery imaging further confirms the clinical viability of the method for volumetric imaging. These results suggest that the proposed F-K method is a promising solution for RCA-based 3D OPW imaging.

Keywords: row–column-addressed arrays, 3D ultrasound imaging, frequency–wavenumber domain processing, orthogonal plane wave compounding

PACS: 43.80.Vj, 43.60.Tj, 87.57.nf, 43.60.Fg

DOI: 10.1088/1674-1056/ae1e67 **CSTR:** 32038.14.CPB.ae1e67

1. Introduction

Three-dimensional (3D) ultrasound imaging can be achieved using two-dimensional (2D) transducer arrays. Traditional fully-sampled 2D matrix arrays require $N \times N$ independent channels,[1,2] where N represents the element number along one side of the probe. This increases the complexity and cost of multi-channel ultrasound systems.[3] To address this challenge, row–column addressed (RCA) arrays have been developed. RCA arrays are a specific type of matrix array consisting of two orthogonal overlapping arrays with elements elongated to match the side length of the probe.[4] Such a design reduces the required number of channels from $N \times N$ to $2N$.[5] RCA arrays have demonstrated advantages in reducing the required channel number and improving the efficiency of 3D volumetric imaging.

Volumetric imaging using RCA arrays has been widely investigated in recent years. Morton[4] first introduced the concept of RCA arrays in 2003. Subsequently, Rasmussen *et al.*[6] performed comparative studies between RCA arrays and fully addressed arrays for volumetric synthetic aperture imaging using simulation data. They further[7] designed roll-off apodization to reduce ghost echo artifacts caused by edge waves. To improve the imaging quality of RCA arrays, Hansen-Shearer *et al.*[8] developed a row–column array specific coherence-based beamforming technique to suppress sidelobes and noise. Zhang *et al.*[9] improved the vascular imaging quality by developing a spatiotemporal similarity weighting method that effectively suppresses sidelobe artifacts. Sun *et al.*[10] proposed the X-FMAS beamforming technique, which uses the spatial coherence of complementary image frames, to suppress the sidelobes and enhance the contrast. Besides, using RCA arrays, Dong *et al.*[11,12] achieved high-volume-rate shear wave elastography with either external vibration or acoustic radiation force (ARF). Re-

[†]These authors contributed equally to this work.
[‡]Corresponding author. E-mail: cjiang17@fudan.edu.cn
[§]Corresponding author. E-mail: xukl@fudan.edu.cn

© 2026 Chinese Physical Society and IOP Publishing Ltd. All rights, including for text and data mining, AI training, and similar technologies, are reserved.

cently, the orthogonal plane-wave (OPW) imaging technique, a specialized emission mode of RCA arrays, has been utilized for high-frame-rate ultrasound imaging. Flesch *et al.*[13] compared the imaging performance of OPW using RCA arrays and plane wave compounding with matrix arrays. They emphasized that OPW compounding is a promising technique for four-dimensional (4D) ultrafast Doppler imaging. Sauvage *et al.*[14] realized 4D ultrafast power Doppler imaging by designing a large aperture probe using the OPW strategy. Sauvage *et al.*[15] further applied the OPW technique to functional ultrasound imaging to monitor the blood flow in the brain. Holbek *et al.*[16] developed a 3D vector flow estimation method using the transverse oscillation technique with RCA arrays. Hansen-Shearer *et al.*[17] and Jensen *et al.*[18] developed OPW-based 3D super-resolution techniques, achieving micron-level precision imaging. Our group has also conducted several research studies on Doppler and super-resolution imaging using OPW with RCA arrays. Sun *et al.*[19] developed a least-squares multi-angle Doppler estimator to achieve 4D vector Doppler imaging based on OPW transmission. Sun *et al.*[20] applied single crystal RCA arrays[21] to 3D ultrasound localization microscopy of rat brain microvasculature. These studies demonstrate the potential of OPW with RCA arrays for 3D applications.

OPW imaging with RCA arrays plays an important role in high-frame-rate volumetric imaging. However, current OPW implementations predominantly rely on conventional delay-and-sum (DAS) algorithms, which suffer from high computational complexity. Although advanced methods such as two-stage beamforming,[22] GPU acceleration,[23] and deep learning techniques[24,25] have partially alleviated the computational burden, developing highly efficient beamforming algorithms remains a challenge for achieving OPW 3D imaging. Frequency–wavenumber (f-k) beamformers have been proven to be a reliable solution to reduce computational burden. Theoretically, the computational complexity of those f-k beamformers is usually reduced by a polynomial order when compared with their DAS counterparts. The f-k beamformer was initially proposed by Stolt for seismic imaging.[26] Then, Lu[27] introduced the high frame rate ultrasound imaging utilizing limited diffraction beams (plane waves) and proposed the corresponding f-k beamforming algorithm. Hunter *et al.*[28] proposed the f-k ultrasound beamforming algorithm for full-matrix capture imaging in ultrasonic non-destructive testing, achieving improvements in both computational efficiency and imaging quality. Garcia *et al.*[29] introduced the f-k beamformer for compounded plane wave imaging, by adapting the tilted plane wave transmission to the conventional explosion model using coordinate transformation. The computational efficiency of Garcia's algorithm is comparable to Lu's method and improves by a polynomial order compared to the DAS method. Zhang *et al.*[30] extended the f-k beamforming to diverging wave-based ultrafast imaging by establishing an isomorphism between planar systems and sectorial systems, enabling the f-k methods to process wide-angle sectorial scans. Merabet *et al.*[31] extended the 2D f-k beamforming to the 3D case using conventional matrix arrays, and they achieved computational efficiency improvements of up to 36 times. Zhuang *et al.*[32] conducted a comparison between the DAS and f-k beamforming for total focusing method and plane wave imaging in non-destructive testing, demonstrating that the f-k beamformer is superior to the DAS algorithms for large image dimensions. Jin *et al.*[33] adopted the f-k method for multilayered structure ultrasound imaging using full matrix data, proving that the f-k method is superior to DAS and phase shift migration. Jiang *et al.*[34] proposed the f-k beamformer for conventional focused transmission-based ultrasound imaging. Lin *et al.*[35] proposed a Fourier-based imaging method using synthetic aperture data acquired from RCA arrays. More recently, Hagemeyer *et al.*[36] developed a frequency-domain filtered back-projection (FBP) reconstruction algorithm for plane wave imaging with RCAs. Currently, the f-k migration algorithm for OPW imaging using RCA arrays remains to be developed.

This paper presents the f-k migration for OPW imaging using RCA arrays, referred to as OPW f-k. This method innovatively concentrates on the wavefront propagation within each cross-section in the orthogonal direction of the plane wave emission plane. The relationship between the radio frequency (RF) data and the response of the free space scatterers in the spectrum domain is then established for those cross-sections. The subsequent sections are organized as follows: Section 2 introduces the theory and the detailed implementation of the proposed OPW f-k migration method; Section 3 describes the simulation setting, experimental setup, and evaluation methods; Section 4 presents simulation, phantom, and *in vivo* experimental results and analysis; Section 5 discusses the innovations and limitations of this research; finally, Section 6 summarizes the paper and outlines future research directions.

2. Theory and method

This section introduces two 3D reconstruction methods for OPW coherent compounded ultrasound imaging using RCA arrays. First, the transmission and reception processes in OPW coherent compounding are introduced. Second, the conventional DAS algorithm adapted for the OPW transmission modality is presented. Finally, the proposed f-k migration method, OPW f-k, is explained in detail.

2.1. Orthogonal plane-wave coherent compounding

In a 2D imaging system, coherent plane wave compounded imaging[13] differs from traditional focused transmis-

sion by emitting a series of tilted plane waves at various angles and coherently compounding the beamformed data from each angle. This approach improves the frame rate by transmitting fewer waves to cover the imaging region, compared to the traditional focused transmission.

When coherent plane wave compounding is applied to RCA arrays, plane waves are generated by sequentially exciting all elements of either the row or column array to insonify the imaging region (Fig. 1(a)), and all elements from the corresponding orthogonal array receive the backscattered ultrasound signals to realize 3D ultrasound imaging (Fig. 1(c)). The insonification angles are typically symmetric around the central axis. Accordingly, for a given maximum steering angle, the transmitted plane waves are usually evenly distributed within the range $[-\theta_{\max}, \theta_{\max}]$. In this case, the point spread function (PSF) is anisotropic, as transmission focusing is achieved through the coherent compounding of tilted plane waves and reception focusing relies on synthetic aperture focusing. To overcome the anisotropic limitation, orthogonal plane wave (OPW) imaging was developed. OPW imaging uses complementary orthogonal plane wave sequences, i.e., row transmission column reception mode (RC) and column transmission row reception (CR) modes. By summing the two orthogonal sequences, the PSFs become isotropic and the final image achieves uniform resolution. This strategy effectively solves the PSF anisotropy problem and provides 3D ultrasound imaging with uniform spatial resolution using RCA probes.

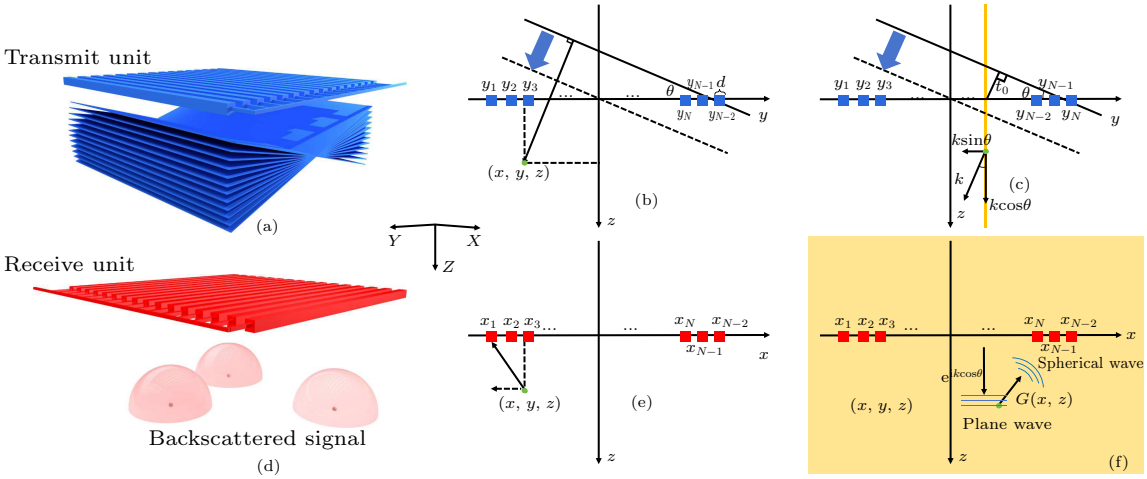


Fig. 1. Illustration of RCA array structure and imaging principles in RC mode: (a) row elements aligned along y-direction transmit tilted plane waves, (d) column elements aligned along x-direction receive RF data, (b) time delay calculation for plane wave transmission at angle θ, (e) time delay calculation for reception, (c) wavenumber analysis during transmission, (f) wavenumber analysis during reception.

2.2. Delay and sum beamforming

DAS beamforming is a conventional algorithm in pulse-echo ultrasound imaging systems for reconstructing ultrasound images from radio-frequency (RF) data acquired by multichannel systems. DAS can focus on a specific point by applying time delays to each received signal so that they align in phase when originating from the point. Those in-phase signals are summed, enhancing the desired signal while suppressing the signal from other directions.

In OPW ultrasound imaging, the imaging coordinate is defined with its origin located at the center of the aperture. Using the RC mode as an example, when the row element arrays transmit a plane wave at a tilt angle of θ, the travelling time of the wavefront from the first transmitting element of the row array to the spatial point (x,y,z), as shown in Fig. 1(b), can be expressed as

$$t_t(x,y,z) = \frac{z\cos\theta + y\sin\theta + (N-1)d/2}{c}, \tag{1}$$

where c is the sound speed, d is the pitch size, and N is the element number. After the wavefront is reflected by the scatterer located at the above-mentioned spatial point, it will propagate backwards to the column elements as illustrated in Fig. 1(e). The travelling time (first arrival) from the spatial point to the column element is

$$t_r(x,y,z) = \frac{\sqrt{z^2 + (x-x_i)^2}}{c}. \tag{2}$$

Now, the total time delay can be expressed as

$$t(x,y,z) = t_t(x,y,z) + t_r(x,y,z). \tag{3}$$

Notably, the time delay is only valid when the spatial point (x,y,z) is inside the aperture; that is, $|x| < (N-1)d/2$ and $|y| < (N-1)d/2$. For the spatial points located outside the aperture, readers can refer to Rasmussen's paper for detailed information.[6,7]

The DAS beamforming is achieved by summing up the delayed RF data in in-phase and quadrature (IQ) mode and coherently compounding the OPW transmissions, as

$$f_{\text{das-rc}}(x,y,z) = \sum_{j=-\theta_0}^{\theta_0} \sum_{i=1}^{N} IQ_{ij}\left(t_{\text{sequence}}, t_{ij}(x,y,z)\right), \tag{4}$$

where i is the received element of the column array, j is the transmitting plane wave from the row array, t_{sequence} is the sampled time sequence of the IQ data, t_{ij} is the total time delay, and θ_0 is the maximum tilted angle. Here, linear interpolation is used to acquire the time-delayed IQ data. Similarly, the beamformed data $f_{\text{das-cr}}(x,y,z)$ can be acquired using the column-transmission row-reception mode. The final beamformed data can be synthesized by summing up the complementary orthogonal sequences as

$$f_{\text{das}}(x,y,z) = f_{\text{das-rc}}(x,y,z) + f_{\text{das-cr}}(x,y,z). \tag{5}$$

Notably, all elements were used for DAS beamforming. No apodization was involved in either transmission or reception in this study.

2.3. F-K migration

The critical factor to realize f-k migration is to find the relationship between the RF data and the response of the free space scatterers in the spectrum domain. To do so, in the proposed OPW f-k, the wave propagation is analyzed in the cross-sections along the plane perpendicular to the receiving array. In this context, RC mode is used as an example. In the 3D coordinate system, the transmitted plane wave front in the frequency domain can be expressed as

$$\Phi_{\text{RT}}(y,z,\omega) = \mathrm{e}^{\mathrm{i}k\sin\theta y + \mathrm{i}k\cos\theta z}, \tag{6}$$

where $k = \omega/c$ is the wavenumber, θ is the tilted angle of the plane wave, and $\mathrm{i} = \sqrt{-1}$ is the imaginary unit, as shown in Fig. 1(c). Correspondingly, the frequency-domain wavefield received by the column element located at x_i, as reflected from the scattering point (x,y,z), can be expressed based on the Green's function, as

$$\Phi_{\text{CR}}(x-x_i,z,\omega) = \frac{\mathrm{i}}{4\pi}\int \frac{\mathrm{e}^{\mathrm{i}(k_x(x-x_i)+k_z z)}}{k_z}\mathrm{d}k_x, \tag{7}$$

where $f(x,z)$ is the intensity of point scatters and t_0 is the travelling time from the first transmitting element of the row array to the above mentioned cross-section at y, as shown in Fig. 1(c).

As indicated in Eq. (8), the received ultrasound response of the imaging system results from the superposition of the spectral responses of all the spatial scatterers, as

$$\begin{aligned} RF(k_x,\omega) &= \int \Phi(x_i,\omega)\,\mathrm{e}^{\mathrm{i}\omega t_0}\,\mathrm{e}^{\mathrm{i}k_x x_i}\,\mathrm{d}x_i, \\ F(k_X,k_Z) &= \iint f(x,z)\,\mathrm{e}^{\mathrm{i}k_X x + \mathrm{i}k_Z z}\mathrm{d}x\mathrm{d}z, \end{aligned} \tag{8}$$

$$RF(k_x,\omega) = \mathrm{i}/2 \times F(k_X,k_Z)/\sqrt{k^2-k_x^2}, \tag{9}$$

where $F(k_X,k_Z)$ denotes the spatial spectrum of the point scatterers, k_X and k_Z are the corresponding spatial wavenumbers, and $RF(k_x,\omega)$ is the spatiotemporal spectrum of the received ultrasound.

From Eqs. (8) and (9), the relationship between the wavenumber of the received ultrasound and the wavenumber of the point scatterers can be established, as

$$\begin{cases} k_X = k_x, \\ k_Z = \sqrt{k^2-k_x^2} + k\cos\theta. \end{cases} \tag{10}$$

Based on Eq. (10), the relationship between the wavenumber of the free space scatterers and the spectrum can be obtained using the following equations

$$k = \begin{cases} \dfrac{k_X^2+k_Z^2}{2k_Z}, & \theta = 0, \\ \dfrac{-k_Z\cos\theta + \sqrt{k_X^2\sin^2\theta + k_Z^2}}{\sin^2\theta}, & \theta \neq 0. \end{cases} \tag{11}$$

The spatial spectrum of the point scatterers can be obtained from the spatio-temporal spectrum of the received ultrasound in Eq. (11) by applying the Stolt interpolation method, as

$$F(k_X,k_Z) = \mathcal{S}^{-1}\left(-2\mathrm{i}\sqrt{k^2-k_x^2}RF(k_x,\omega)\right), \tag{12}$$

where $\mathcal{S}^{-1}$ is the Stolt remapping.

Figure 2 presents the detailed flowchart illustrating the process of achieving 3D ultrasound imaging using the OPW f-k method in RC mode. The implementation steps are as follows:

(i) For a selected transmitting angle θ, the backscattered signals $RF(x,t)$ in the time-spatial domain are zero-padded and then converted to the wavenumber-frequency domain $RF(k_x,\omega)$ using a 2D fast Fourier transform (FFT).

(ii) For a chosen 2D cross-section y, phase compensation is applied to $RF(k_x,\omega)$ to correct for the travelling time from the first transmitting element to the cross-section y.

(iii) Calculate k for each k_X and k_Z, then apply Stolt interpolation to acquire $F(k_X,k_Z)_y$.

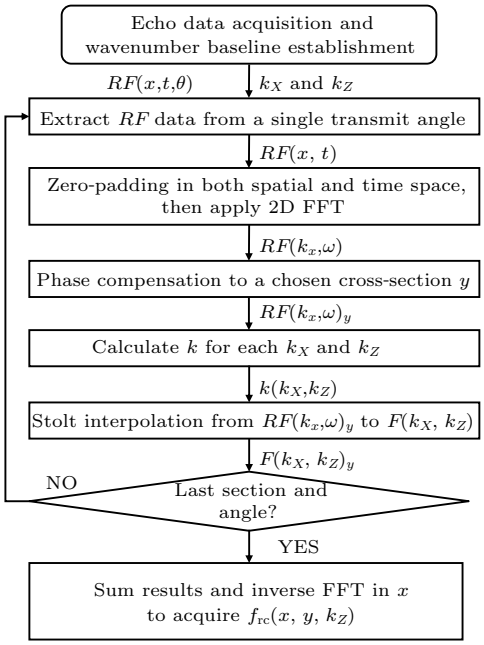


Fig. 2. Flow chart of the OPW f-k algorithm in RC mode.

(iv) The above three steps are repeated for each cross-section and transmission angle until the last section and angle are reached.

(v) The results are summed to achieve coherent compounding, then an inverse FFT is performed in the x direction on the summed data to acquire beamformed data $f_{\mathrm{rc}}(x,y,k_Z)$.

Similarly, the beamformed data can be easily obtained in CR mode. The final beamformed data can be obtained by summing the beamformed data of the two orthogonal sequences, as

$$f(x,y,k_z) = f_{\mathrm{rc}}(x,y,k_Z) + f_{\mathrm{cr}}(x,y,k_Z). \tag{13}$$

The final beamformed image is obtained using 1D FFT in the z direction.

Notably, Stolt interpolation has been thoroughly introduced by Garcia;[29] readers may refer to his paper for further details. In this study, the classical linear interpolation was used, and the corresponding MATLAB code can be expressed as interp1$(\omega, RF, ck,$ 'linear'$)$, where ω is the frequency, RF is the data in the frequency domain at a fixed k_x, ck is the product of sound speed and the synthesized wavenumber in Eq. (11).

2.4. Performance evaluation metrics

Three metrics were used to quantitatively evaluate the algorithm performance. Full width at half maximum (FWHM), defined as the main lobe width at 6 dB below the peak of the PSF curve, was used to evaluate the imaging resolution. Contrast ratio (CR) and contrast-to-noise ratio (CNR) were employed to assess the detectability of targets in ultrasound images for the cyst phantom and *in vivo* experiments, as

$$\mathrm{CR} = 20\log_{10}\left(\frac{u_{\mathrm{i}}}{u_{\mathrm{b}}}\right), \tag{14}$$

$$\mathrm{CNR} = \frac{|u_{\mathrm{i}} - u_{\mathrm{b}}|}{\sqrt{\sigma_{\mathrm{i}}^2 + \sigma_{\mathrm{b}}^2}}, \tag{15}$$

where u_{i} and u_{b} represent the mean gray values of the target and background regions, respectively, and σ_{i} and σ_{b} are their corresponding standard deviations.

3. Experiment setup

The performance of the proposed method was evaluated using simulation experiments, phantom experiments, and in vivo experiments. All experiments were conducted using the multi-channel ultrasound platform (Vantage 256, Verasonics, Inc., WA, USA) and the RC6gV RCA probe (Vermon, Inc., France). The RCA probe contains 128+128 elements. The element pitch is 0.2 mm. The side length of the array is 25.6 mm. The probe operates at a center frequency of 6 MHz. All data were collected at a sampling rate of 25 MHz. A sound speed of 1540 m/s was used for all imaging tests.

The simulations were performed using the 'simulation' mode in the Vantage 256 system. Thirty-one points were arranged according to the default distribution from the Vantage system. They were distributed from -12.7 mm to 12.7 mm in both the lateral and elevation directions, and from 5 mm to 42 mm in the axial direction. The transmitting angles of the plane wave were evenly distributed from -16 degrees to 16 degrees with an increment of 1 degree.[37]

Phantom experiments were conducted using the commercial ultrasound phantom CIRS model 040GSE. The RCA array was sequentially positioned against the wire region first, followed by the cyst region. *In vivo* experiments were performed on the carotid artery of a healthy volunteer. All experiments were conducted using the same platform and parameters, as listed in Table 1. In this study, ultrasound images had a resolution of $128 \times 128 \times 1024$ voxels for all simulations and experiments. The voxels were aligned under the elements of the transducer. The spacing of the voxels was 0.2 mm (less than one wavelength) in the elevation and lateral directions, and 0.0362 mm (about one-seventh of the wavelength) in the axial direction.

Table 1. Parameters of the RCA probe and experimental setup.

Parameter	Value	Unit
No. elements	128+128	–
Element pitch	0.2	mm
Array length	25.6	mm
Center frequency	6	MHz
Sampling frequency	25	MHz
Speed of sound	1540	m/s
Tilted angles	–16:1:16	degree

4. Result

4.1. Point target simulation

Figures 3(a) and 3(e) illustrate the volumetric ultrasound images of scattering points reconstructed using the OPW DAS and OPW f-k methods, respectively. The overall shapes of the scatterers are identical except for the minor difference in artifact distribution between the two methods.

The differences in the point targets are clearly observed from the cross-sectional images of three orthogonal planes. In the lateral-elevation (xy) plane, the image distributions of the two methods exhibit a "cross-shaped snowflake" pattern for the point located at a depth of 23 mm (Fig. 3(b) and Fig. 3(f)). The main difference may lie in the distribution of artifacts. The image distributions exhibit a wing-shaped pattern in the axial-lateral (xz) plane at $y = 0$ mm and in the axial-elevation (yz) plane at $x = 0$ mm. They are nearly identical for the two planes using the OPW-DAS method (Fig. 3(c) and Fig. 3(d)), because the simulated points are almost symmetrically arranged with respect to the centerline of the aperture except for the difference in the number of points at the depth of 8 mm. Such a trend can also be observed for the OPW f-k method (Fig. 3(g) and Fig. 3(h)).

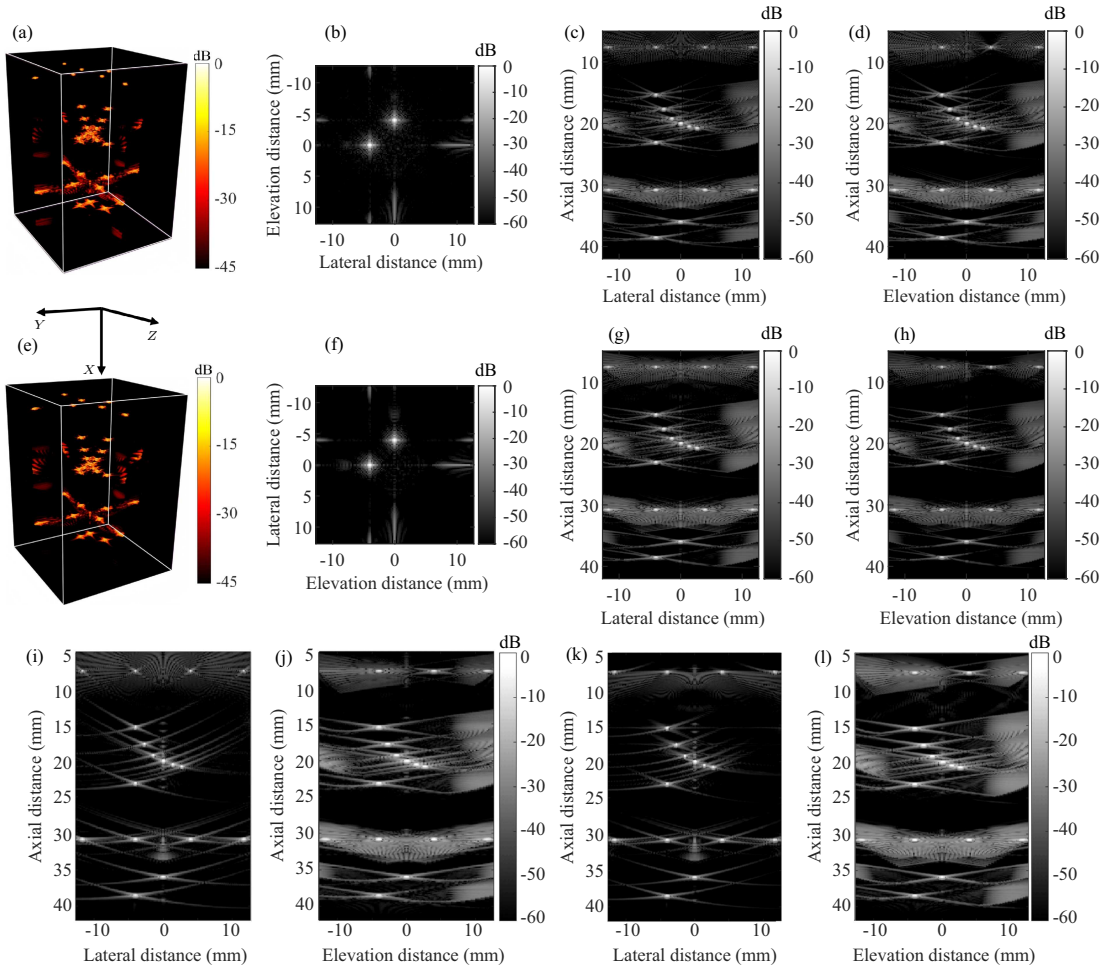


Fig. 3. 3D images of simulated point targets reconstructed by (a) OPW-DAS, (e) OPW f-k. 2D cross-sectional images from 3D images of simulated point targets reconstructed by the OPW-DAS method [(b), (c), (d)] and the OPW f-k method [(f), (g), (h)]. (b) and (f) lateral-elevation slices at a depth of $z = 23$ mm, (c) and (g) axial-lateral slices at $y = 0$ mm, (d) and (h) axial-elevation slices at $x = 0$ mm. Images reconstructed using OPW-DAS and OPW f-k methods in RC mode (i)–(l). Axial-lateral slices reconstructed using (i) OPW-DAS and (k) OPW f-k, axial-elevation slices reconstructed using (j) OPW-DAS, and (l) OPW f-k.

When the axial-lateral plane is selected for comparison, the point images are almost identical at a depth greater than 17 mm for the two methods (Fig. 3(c) and Fig. 3(g)). For the point scatterers located between 0 mm and 17 mm, their positions are accurately determined, but the wing-shaped artifacts are different. To better illustrate the differences in artifacts, the individual imaging results in RC mode are taken out for comparison. It can be seen from Figs. 3(i)–3(l) that point images at a depth of 8 mm exhibit artifacts resembling nearly horizontal straight lines when using OPW f-k, while wing-shaped artifacts persist when using OPW-DAS. Point images at depths of 15 mm and 17 mm show a combination of horizontal straight lines and wing-shaped artifacts (Fig. 3(i) and Fig. 3(k)). This phenomenon also appears in similar f-k algorithms.[35] Such artifacts might be due to the inaccurate remapping when implementing Stolt interpolation. Advanced interpolation methods require investigation to reduce the artifacts. Besides, the artifacts of the points in the axial-elevation plane are nearly identical (Fig. 3(j) and Fig. 3(l)). This is because f-k migration is performed only in the axial-lateral plane, while in the axial-elevation plane, a simple summation is performed. To some extent, the processing in the axial-elevation plane in OPW f-k is the same as that in OPW-DAS. In addition, the PSFs show anisotropy (Fig. 3(k) and Fig. 3(l)), as transmission focusing is achieved through the coherent compounding of tilted plane waves and reception focusing relies on synthetic aperture focusing. When complementary CR mode data is combined with RC mode data in the final image reconstruction, the PSFs become isotropic, and the wing-shaped artifacts are also summed. That is why four pairs of wing-shaped artifacts are visible in Fig. 3.

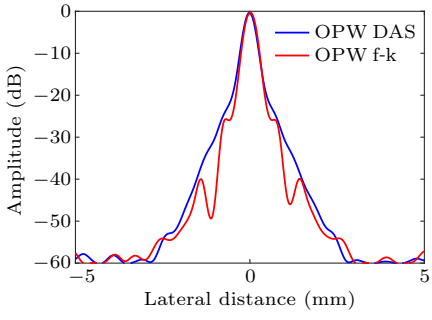


Fig. 4. Lateral profiles of the simulated point targets at a depth of 23 mm.

The lateral profile analysis at a depth of 23 mm demon-

strates the advantages of OPW f-k in terms of main lobe width and sidelobe suppression (Fig. 4). Figure 4 shows lateral profiles from both methods at the same depth, allowing direct comparison of their performance. The OPW f-k method (red line) exhibits a slightly sharper main lobe and superior sidelobe suppression compared to the OPW-DAS method (blue line). This improvement might be due to the ability of frequency–wavenumber domain processing to more accurately characterize the wave propagation physics, rather than relying solely on the geometric approximations used in DAS beamforming.

Quantitative results (Table 2) show that OPW f-k achieves an FWHM of 0.41 ± 0.002 mm, representing an improvement of approximately 1.7% compared to the FWHM of 0.42 ± 0.001 mm achieved by OPW-DAS. Although the improvement in FWHM is modest, it demonstrates better performance across all measured points. This improvement, combined with the superior sidelobe suppression visible in the profiles, confirms the enhanced performance of the proposed method in 3D ultrasound imaging.

Table 2. Performance comparisons of OPW-DAS and OPW f-k methods.

	FWHM (mm)		CR (dB)		CNR	
	OPW-DAS	OPW f-k	OPW-DAS	OPW f-k	OPW-DAS	OPW f-k
Simulated point targets	0.42±0.001	0.41±0.002	–	–	–	–
Wire phantom experiment	0.50±0.029	0.49±0.038	–	–	–	–
Cyst phantom experiment	–	–	7.53	7.78	2.58	3.02
Carotid artery (*in vivo*)	–	–	4.25	5.21	1.45	1.72
Average improvement	2.19%		12.96%		17.84%	

4.2. Wire phantom experiments

Wire phantom experiments were conducted to further validate the performance of the proposed method. The selected region of the CIRS model 040GSE phantom contained multiple point targets and anechoic regions. These point targets were positioned at depths from 10 mm to 42 mm. The three-dimensional reconstruction results show that both methods can clearly reconstruct the target structures (Fig. 5(a)). However, the OPW-DAS method shows better image amplitude for deep targets. This difference might come from their different signal processing approaches. In DAS, RF data from each transmit-receive pair are summed together. This causes signal intensity to increase with depth as more pairs contribute to the image. The f-k method is based on the Green's function in free space, and the ultrasound images are derived from the RF data without this summation process. The intensity difference can be fixed by adjusting the time gain compensation (TGC) parameters. The cross-sectional images from three orthogonal planes validate the accurate positioning of the speckle wires and speckle cylinders (Fig. 5). The cross-sectional images obtained from both methods exhibit a high similarity, except for the presence of two line-shaped artifacts near the surface in the OPW-DAS method (Fig. 5(d)).

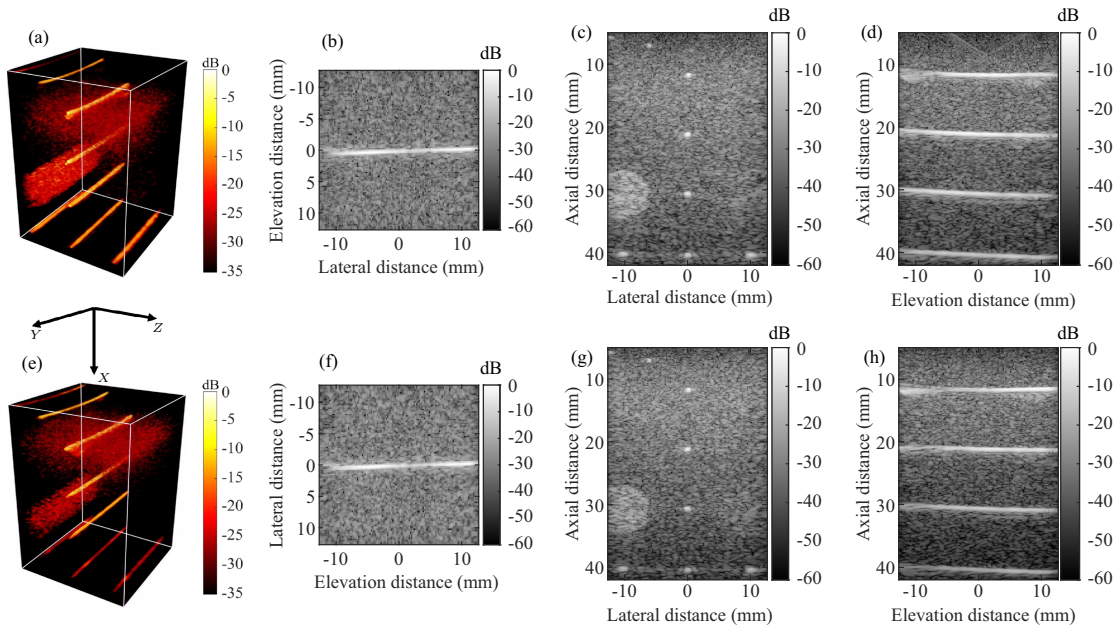


Fig. 5. 3D images of wire phantom reconstructed by (a) OPW-DAS, (e) OPW f-k. 2D slices from 3D phantom images reconstructed using [(b), (c), (d)] OPW-DAS and [(f), (g), (h)] OPW f-k. (b) and (f) Lateral-elevation slices at a depth of $z = 22$ mm, (c) and (g) axial-lateral slices at $y = 0$ mm, (d) and (h) axial-elevation slices at $x = 0$ mm.

Quantitative results of the lateral −6-dB FWHM, averaged across all four point targets visible in Fig. 5(g), which are on the axis line, show that OPW f-k achieves a mean FWHM of 0.49 ± 0.038 mm (Table 2), representing an improvement of approximately 3.0% compared to OPW-DAS's 0.50 ± 0.029 mm. Notably, the improvement in FWHM is most pronounced for shallower targets with a 6.1% improvement at 11.7-mm depth, compared to deeper targets. This observation suggests that the frequency–wavenumber domain processing offers particular advantages in the near field where conventional DAS beamforming is inherently limited by resolution constraints.

4.3. Cyst phantom experiments

The ultrasound phantom containing anechoic cyst regions was used to assess the contrast performance of the proposed method. Figures 6(a) and 6(e) show the volumetric ultrasound image of a cyst at a depth of 30 mm, where both methods clearly delineate the shape and boundaries of the cyst cylinder. The OPW-DAS method exhibits higher brightness in deeper regions than OPW f-k. Such a trend has been described in the wire phantom experiment. Figures 6(b)–6(d) and 6(f)–6(h) further illustrate the detailed characteristics of cyst imaging through lateral-elevation, axial-elevation, and axial-lateral slices. To evaluate both methods, CR and CNR values were calculated. The cyst regions used for calculating these metrics are marked with red circles, while the speckle regions are marked with blue circles.

Quantitative results (Table 2) show that the OPW f-k method can achieve improvements in contrast metrics: the CR increased from 7.53 dB to 7.78 dB, an improvement of approximately 3.3%; the CNR improved from 2.58 to 3.02, an increase of about 17.1%. These improvements primarily result from the advantages of frequency–wavenumber domain processing in background noise suppression. The improved CNR indicates that OPW f-k provides better differentiation between the cyst and surrounding tissue even in the presence of speckle noise.

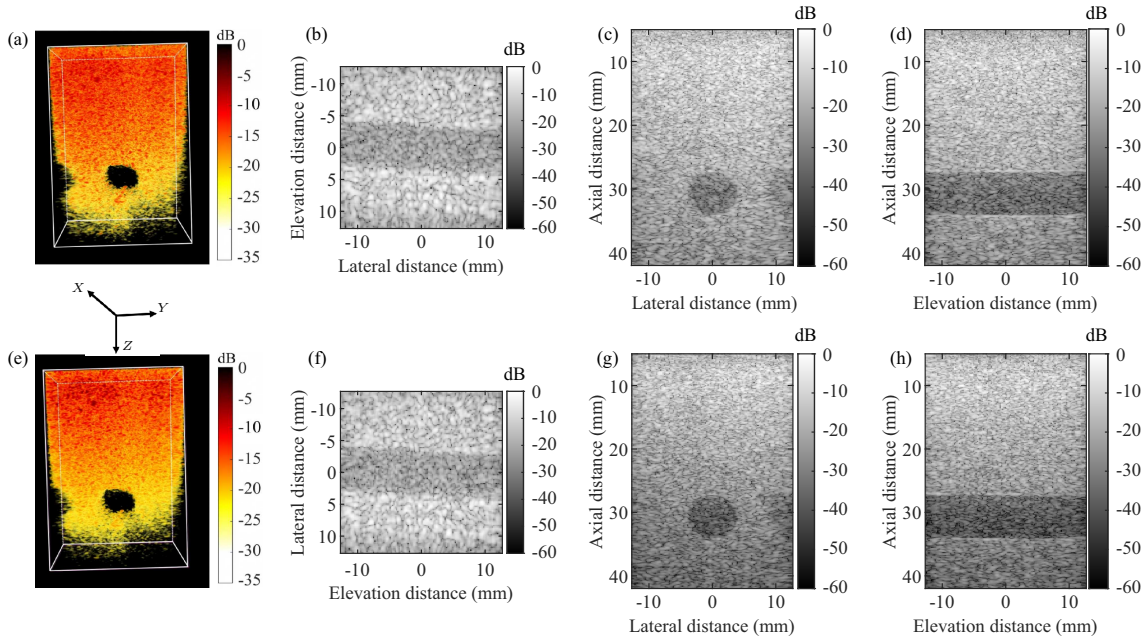


Fig. 6. 3D images of cyst phantom reconstructed by (a) OPW-DAS and (e) OPW f-k methods. 2D slices from 3D phantom images reconstructed using [(b), (c), (d)] OPW-DAS and [(f), (g), (h)] OPW f-k methods. (b) and (f) Lateral-elevation slices at a depth of $z = 30$ mm, (c) and (g) axial-lateral slices at $y = 0$ mm, (d) and (h) axial-elevation slices at $x = 0$ mm.

4.4. *In vivo* experiments

To further validate the feasibility of the proposed method in clinical applications, an *in vivo* experiment was conducted on a healthy volunteer focusing on imaging the carotid artery. This study was approved by the Human Research Ethics Committee, Huashan Hospital affiliated with Fudan University (Application No. 2021-065). The volunteer was positioned supine, with the probe placed on one side of the neck to acquire volumetric images of the carotid artery. It can be seen from Fig. 7 that both methods successfully reconstructed the basic anatomical structure of the carotid artery. The position and morphology of the vessel lumen are clearly visible. Figures 7(a) and 7(d) demonstrate volumetric ultrasound images of the two methods. The carotid artery is visible for both methods, except for the lower imaging intensity in deeper regions in OPW f-k. In the axial-lateral plane (Fig. 7(b) and Fig. 7(e)) and axial-elevation plane (Fig. 7(c) and Fig. 7(f)), both methods clearly display the vessel lumen and surrounding tissue structures. Imaging performance was evaluated by comparing the contrast between the carotid artery lumen (marked by a blue circle) and the surrounding tissue (marked by a red circle). Quantitative results (Table 2) show that the OPW f-k method achieves a CR approximately 22.7% higher (5.21 dB *versus* 4.25 dB), and a CNR approximately 18.2% greater

(1.72 *versus* 1.45) than that of the OPW-DAS method.

These improvements indicate the great potential of the OPW f-k method for in vivo vascular imaging. The superior performance in superficial structures like the carotid artery suggests that the frequency–wavenumber domain processing may be particularly advantageous for imaging shallow anatomical structures, where conventional DAS beamforming faces challenges with near-field effects. Once again, it can be observed from the images that the OPW f-k method demonstrates relatively weaker signal intensity in deeper tissues. This issue can be addressed by appropriately adjusting the TGC configuration.

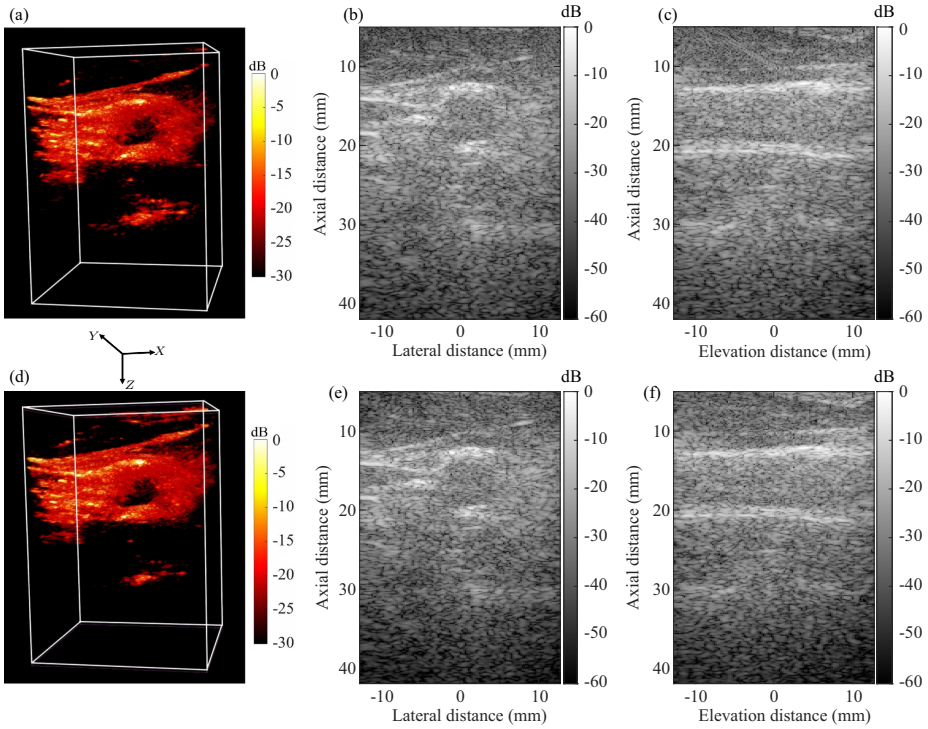


Fig. 7. The 3D images of human carotid artery reconstructed using (a) OPW-DAS, (d) OPW f-k. Axial-lateral slices at $y = 0$ mm using (b) OPW-DAS and (e) OPW f-k, axial-elevation slices at $x = 0$ mm using (c) OPW-DAS and (f) OPW f-k.

4.5. Computational complexity analysis

To analyze the computational advantages of the OPW f-k method over the traditional DAS algorithm, a detailed evaluation of computational complexity was performed for both methods. Assume N is the number of elements in each direction of the RCA probe, K is the number of time samples, P is the number of transmission angles, M is the number of axial imaging voxels, and H is the number of lateral/elevational imaging voxels. Here, only the CR mode is analyzed. For the OPW-DAS algorithm, the receive delay calculation requires $a_1 \times N \times M \times H^2$ operations, where a_1 is about 6 because of addition, subtraction, multiplication, square root, and division operations. For each transmission angle, the transmit delay calculation requires $a_2 \times M \times H^2$ operations, where a_2 is about 6 because of trigonometric functions, addition, and division functions. For each of the N transmission and receive channels, the algorithm requires $M \times H^2$ delay calculations, $12 \times M \times H^2$ linear interpolation operations (12 basic arithmetic operations considering complex numbers), and $2 \times M \times H^2$ data accumulations (considering complex numbers). Therefore, OPW-DAS requires about $15 \times P \times N \times M \times H^2 + 6 \times (P+N) \times M \times H^2$ basic arithmetic operations. The computational complexity of OPW-DAS is $O(PNMH^2)$.

For the proposed OPW f-k algorithm, the computational complexity of one tilted angle wave transmission and one cross section beamforming is first analyzed. The f-k beamformer begins with a 2D FFT applied to both time and spatial samples, requiring approximately $c \times K \times N \times \log_2(K \times N)$ operations. Here, c is a constant between 30 and 50 because of the radix-2 FFT, as well as zero-padding in both the spatial and temporal directions. Phase compensation requires about $c_1 \times K$ operations, where c_1 is a constant between 1.5 and 2.5 because of the band-passed spectrum and complex numbers. The Stolt remapping step is computationally intensive. Wavenumber calculation requires $c_2 \times M \times H$ operations for each tilted angle, where c_2 is 7 or 10. Linear interpolation in the frequency domain requires $24 \times M \times H$ operations for each tilted angle and cross-section, considering zero-padding in the spatial domain and complex numbers. Finally, the 1D inverse FFT in the spatial direction requires $5 \times M \times H \times \log_2(H)$ operations. The total arithmetic operations are $c \times P \times K \times N \times \log_2(K \times N) + c_1 \times P \times N \times K + c_2 \times P \times M \times H + 12 \times P \times N \times M \times H + 5 \times P \times N \times M \times \log_2(H)$ (Table 3). Notably, H is generally equal to N, and K is about one-fourth the value of M because of zero-padding in the f-k beamformer. The computational complexity is $O(PMH^2 \log_2(MH))$ for OPW f-k.

Table 3. Computational complexity of the imaging algorithms.

Operation	Algorithm	
	OPW-DAS	OPW f-k
Receive delay calculation	$6\times N\times M\times H^2$	–
Transmit delay calculation	$6\times P\times M\times H^2$	–
Linear interpolation	$15\times P\times N\times M\times H^2$	–
2D FFT	–	$c\times P\times K\times N^2\times\log_2(K\times N)$
Phase compensation	–	$c_1\times P\times N\times K$
Stolt remapping	–	$c_2\times P\times M\times H+24\times P\times N\times M\times H$
1D IFFT	–	$5\times P\times N\times M\times H\times\log_2(H)$
Computational complexity	$O(PNMH^2)$	$O(PMH^2\log_2(MH))$

In practice, the OPW f-k algorithm demonstrated approximately an 11-fold performance improvement over the OPW-DAS algorithm with an imaging voxel size of $128\times128\times1024$ using MATLAB on a standard workstation (12th Gen Intel(R) Core(TM) i7-12700 2.10 GHz, 128 GB). The processing time improvement might vary depending on the computing platform and low-level programming language.

Furthermore, when the voxel number is fixed at 128 in both the lateral and elevational directions, the computational times were recorded as the number of voxels in the axial direction increased from 256 to 8192 (Fig. 8). The results show that the computational advantages of OPW f-k over OPW-DAS become more pronounced as the voxel number increases. This suggests that OPW f-k is well suited for large-scale 3D ultrasound imaging applications.

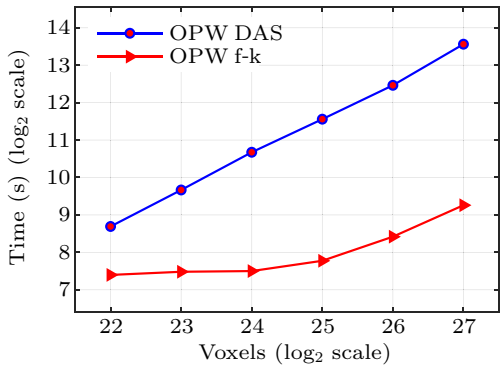


Fig. 8. Computational time comparison as a function of the number of voxels between OPW-DAS and OPW f-k.

5. Discussion

This study presents a frequency–wavenumber domain migration strategy for OPW ultrasound imaging using RCA arrays. Both simulation and experimental results demonstrate that the proposed OPW f-k method can achieve improved spatial resolution and contrast while significantly enhancing computational efficiency compared with the traditional DAS method. Quantitative results demonstrate an average improvement of 2.19% in FWHM. The average enhancements in contrast ratio (CR) and contrast-to-noise ratio (CNR) are 12.96% and 17.84%, respectively.

From the point target simulation and phantom experiments, it is evident that OPW f-k exhibits superior performance in main-lobe width reduction and sidelobe suppression compared to OPW-DAS. The performance difference may be attributed to their different theoretical foundations. OPW-DAS relies on geometric approximations, calculating delays based on straight-line propagation paths between transducer elements and imaging points. While this approach is intuitive and has proven effective in practice, it may not fully account for complex wave propagation phenomena. In contrast, OPW f-k processes the data in the frequency–wavenumber domain, where the wave equation naturally describes the physics of wave propagation. The f-k migration algorithm used in OPW f-k provides a more accurate mathematical solution to the inverse problem by properly accounting for the dispersion relationship in wave propagation, leading to improved resolution and reduced artifacts. Imaging resolution can be further improved by using the full-waveform inversion (FWI) method.[38,39]

The proposed method has several limitations. First, the proposed method only works when the imaging space is within the aperture. This means that the field of view is limited. Second, the method's performance in deep tissue imaging needs further optimization, possibly through improved gain compensation strategies or adaptive processing techniques. Third, the proposed f-k method requires more memory than its DAS counterparts to store the zero-padded RF data and the intermediate variables, which might introduce hardware burdens.

6. Conclusion

This paper has proposed a frequency–wavenumber domain migration method for orthogonal plane wave imaging with row–column-addressed arrays. The proposed OPW f-k method was evaluated using point simulations, phantom experiments, and *in vivo* experiments. The quantitative results show that OPW f-k achieves superior spatial resolution and enhanced contrast performance while reducing computational complexity compared to the DAS algorithm. The proposed method demonstrates a promising technique for real-time orthogonal plane wave compounded imaging with row–column-

addressed arrays.

Acknowledgements

Project supported by the National Key Research and Development Program of China (Grant No. 2023YFC2410900) and the National Natural Science Foundation of China (Grant Nos. 12574495 and 12204113).

References

[1] Seo C H and Yen J T 2009 *IEEE Trans. Ultrason. Ferroelectr. Freq. Control* **56** 837
[2] Logan A S, Wong L L P, Chen A I H and Yeow J T W 2011 *IEEE Trans. Ultrason. Ferroelectr. Freq. Control* **58** 1266
[3] Castrignano L, Tortoli P, Matrone G, Crocco M, Savoia A S and Ramalli A 2025 *IEEE Trans. Biomed. Eng.* **72** 1941
[4] Morton C E and Lockwood G R 2003 *Proceedings of the IEEE Ultrasonics Symposium* p. 968
[5] Wang N, Qiang Y, Qiu C, Chen Y, Wang X, Pan Y, Liu R, Wu W, Zheng H, Qiu W and Zhang Z 2024 *IEEE Trans. Biomed. Eng.* **71** 831
[6] Rasmussen M F, Christiansen T L, Thomsen E V and Jensen J A 2015 *IEEE Trans. Ultrason. Ferroelectr. Freq. Control* **62** 947
[7] Rasmussen M F and Jensen J A 2013 *Proc. SPIE Medical Imaging: Ultrasonic Imaging, Tomography, and Therapy* **8675** 73
[8] Hansen-Shearer J, Lerendegui M, Toulemonde M and Tang M 2022 *IEEE Trans. Ultrason. Ferroelectr. Freq. Control* **69** 480
[9] Zhang J, Huang C, Lok U, Dong Z, Liu H, Gong P, Song P and Chen S 2025 *IEEE Trans. Med. Imaging* **44** 297
[10] Sun Q, Fu Y and Xu K 2023 *Proc. IEEE Int. Ultrason. Symp. (IUS)* p. 1
[11] Dong Z, Kim J, Huang C, Lowerison M R, Lok U, Chen S and Song P 2022 *BME Frontiers* **2022** 9874863
[12] Dong Z, Lok U, Lowerison M R, Huang C, Chen S and Song P 2024 *IEEE Trans. Ultrason. Ferroelectr. Freq. Control* **71** 448
[13] Flesch M, Pernot M, Provost J, Ferin G, Nguyen-Dinh A, Tanter M and Deffieux T 2017 *Phys. Med. Biol.* **62** 4571
[14] Sauvage J, Flesch M, Ferin G, Nguyen-Dinh A, Poree J, Tanter M, Pernot M and Deffieux T 2018 *Phys. Med. Biol.* **63** 215012
[15] Sauvage J, Poree J, Rabut C, Ferin G, Flesch M, Rosinski B, Nguyen-Dinh A, Tanter M, Pernot M and Deffieux T 2020 *IEEE Trans. Med. Imaging* **39** 1884
[16] Holbek S, Christiansen T L, Stuart M B, Beers C, Thomsen E V and Jensen J A 2016 *IEEE Trans. Ultrason. Ferroelectr. Freq. Control* **63** 1799
[17] Hansen-Shearer J, Yan J, Lerendegui M, Huang B, Toulemonde M, Riemer K, Tan Q, Tonko J, Weinberg P D and Dunsby C 2024 *Ultrasound Med. Biol.* **50** 1045
[18] Jensen J A, Ommen M L, Øygard S H, Schou M, Sams T, Stuart M B, Beers C, Thomsen E V, Larsen N B and Tomov B G 2019 *IEEE Trans. Ultrason. Ferroelectr. Freq. Control* **67** 538
[19] Sun Q, Fu Y, Yan S and Xu K 2025 *IEEE Trans. Ultrason. Ferroelectr. Freq. Control* **72** 202
[20] Sun Q, Hou S, He R, Fu Y, Wu J, Dai J and Xu K 2025 *IEEE Trans. Ultrason. Ferroelectr. Freq. Control* **72** 698
[21] Li G, Sun Q, Fu Y, Hou S, Zhang J, Xu K L and Dai J Y 2024 *Ultrasonics* **139** 107289
[22] Jørgensen L T, Præsius S K, Stuart M B and Jensen J A 2023 *IEEE Trans. Ultrason. Ferroelectr. Freq. Control* **70** 668
[23] Stuart M B, Jensen P M, Olsen J T R, Kristensen A B, Schou M, Dammann B, Sorensen H H B and Jensen J A 2021 *IEEE Trans. Ultrason. Ferroelectr. Freq. Control* **68** 2608
[24] Lian Y, Zeng Y, Zhou S, Zhu H, Li F and Cai X 2025 *IEEE Trans. Ultrason. Ferroelectr. Freq. Control* **72** 226
[25] Wang P, Ma H, Liu T, Liu C, Li D and Ta D 2025 *Chin. Phys. B* **34** 044301
[26] Stolt R H 1978 *Geophysics* **43** 23
[27] Lu J 1997 *IEEE Trans. Ultrason. Ferroelectr. Freq. Control* **44** 839
[28] Hunter A J, Drinkwater B W and Wilcox P D 2008 *IEEE Trans. Ultrason. Ferroelectr. Freq. Control* **55** 2450
[29] Garcia D, Tarnec L L, Muth S, Montagnon E, Poree J and Cloutier G 2013 *IEEE Trans. Ultrason. Ferroelectr. Freq. Control* **60** 1853
[30] Zhang M, Varray F, Besson A, Carrillo R E, Viallon M, Garcia D, Thiran J, Liebgott H and Bernard O 2016 *IEEE Trans. Ultrason. Ferroelectr. Freq. Control* **63** 2125
[31] Merabet L, Robert S and Prada C 2019 *IEEE Trans. Ultrason. Ferroelectr. Freq. Control* **66** 772
[32] Zhuang Z, Zhang J, Lian G and Drinkwater B W 2020 *Sensors* **20** 4951
[33] Jin H and Chen J 2021 *Mech. Syst. Signal Process.* **149** 107149
[34] Jiang C, Liu C, Zhan Y and Ta D 2022 *Ultrason. Imaging* **44** 59
[35] Lin S C and Li P C 2024 *IEEE Trans. Ultrason. Ferroelectr. Freq. Control* **71** 85
[36] Hagemeyer P, Lisson T, Dencks S and Schmitz G 2024 *2024 IEEE Int. Symp. Biomed. Imaging (ISBI)* p. 1
[37] Fu Y P, Sun Q D, Li B Y, Ta D A and Xu K L 2023 *Acta Phys. Sin.* **72** 074302 (in Chinese)
[38] Li Y F, Shi Q Z, Li Y, Song X J, Liu C C, Ta D and Wang W Q 2021 *Chin. Phys. B* **30** 014302
[39] Li P P, Li Y B, Su C, Dong Z Y and Lin W J 2025 *Chin. Phys. B* **34** 054301